Thin Solid Films 769 (2023) 139741

Contents lists available at ScienceDirect

Thin Solid Films

journal homepage: www.elsevier.com/locate/tsf

Optical modeling and analysis of pixel organic light-emitting diode using a mixed-level algorithm considering light leakage effects

Linya Chen [a,b], Honggang Gu [c,*,1], Shibo Jiao [d], Shiyuan Liu [a,c]

[a] School of Optical and Electronic Information, Huazhong University of Science and Technology, Wuhan, Hubei 430074, China
[b] Innovation Institute, Huazhong University of Science and Technology, Wuhan, Hubei 430074, China
[c] State Key Laboratory of Digital Manufacturing Equipment and Technology, Huazhong University of Science and Technology, Wuhan, Hubei 430074, China
[d] Shenzhen China Star Optoelectronics Semiconductor Display Technology Co., Ltd., Shenzhen, Guangdong 518132, China

ARTICLE INFO

Keywords:
Pixel organic light-emitting diodes
Mixed-level algorithm
Light leakage effects
Ray tracing

ABSTRACT

Fast optical simulation is the basis of optical optimization for cross-scale 3D pixel organic light-emitting diodes (OLEDs), and it is among the most critical challenges in the industry. We constructed an optical simulation model by using a mixed-level algorithm to fasten the analysis of pixel OLEDs, considering the light leakage effect, which was described in terms of the ratio of light extraction (*RLE*). Model correctness and efficiency were verified using a commercial software. Pixel OLEDs with different sizes were used, and the influence of the height and angle of pixel definition layers (PDLs) and width of color filters on the performance was analyzed. These geometric features change the path of light propagation, which changes performance. Device B was more sensitive to the PDL angle, whereas devices A and C were more sensitive to the PDL height. Device B had the least *RLE* ($RLE_B > RLE_A > RLE_C$). An optimal structure can reduce light leakage and improve the performance of pixel OLEDs. The proposed method provides guidelines for designing optimal pixel OLEDs and for the high-throughput simulation of pixel OLEDs.

1. Introduction

Organic light-emitting diodes (OLEDs) have been widely used in mobile devices, displays, and lighting because of their unique advantages, such as wide viewing angles, fast response time, and high contrast ratios [1–3]. However, contemporary research still relies on the trial-and-error method, which is expensive and time-consuming [4]. Compared to trial-and-error methodology, optical simulation models have several advantages; for example, they can help understand the physical mechanism of OLEDs and are less expensive and time-consuming. Thus, optical simulation is an indispensable tool for guiding the design of OLEDs [5,6]. A simple monochromatic OLED device typically uses a stratified structure comprising multilayer thin films. Most studies have focused on such OLEDs [7,8]; meanwhile, several well-established optical models have been proposed to analyze their key optical performance [5,9,10]. Researchers have also used experiments and optical models to propose valuable ways to improve device performance [11–13]. Since most displays tend to be colorful, monochromatic OLEDs are not sufficient, and devices containing diverse colors are required. For a complete pixel OLED that can present various colors, at least three monochromatic OLEDs should be included, namely the red, blue, and green subpixels [14–16]. During fabrication, pixel definition layers (PDLs) are used between subpixels to prevent luminescent materials from mixing with adjacent subpixels; however, this limits the dimension of the horizontal direction. Furthermore, thick encapsulation layers are introduced to improve lifetime and overcome degradation, which expands the scale of vertical dimensions from nanometers to micrometers. Color filter (CF) arrays are also used and separated by black matrixes (BMs) in high-resolution OLEDs [17,18]. These complex features lead to an across-scale pixel OLED devices with three-dimensional (3D) structures; as a result, the multilayer optical model for simple stratified monochromatic OLEDs has become archaic.

A few studies have conducted optical modeling and analysis for pixel OLEDs. In 2014, Chang et al. first proposed a mixed-level algorithm that unifies the advantages of ray optics and wave optics, laying the foundation for the optical modeling of cross-scale OLEDs [19]. However,

* Corresponding author.
E-mail address: hongganggu@hust.edu.cn (H. Gu).
[1] Present Address: Nanoscale and Optical Metrology Group, School of Mechanical Science and Engineering, Huazhong University of Science and Technology, Luoyu Road 1037, Wuhan, Hubei 430074, China.

https://doi.org/10.1016/j.tsf.2023.139741
Received 28 September 2022; Received in revised form 13 February 2023; Accepted 14 February 2023
Available online 16 February 2023

combining wave optics and ray optics requires a near-to-far-field (NTFF) transformation method. Kane et al. also used this method to analyze the performance of stratified OLEDs with a Moth's eye grating pattern at the glass–air interface [20]. They used rigorous electromagnetic (EM) methods based on wave optics, such as finite-difference time-domain (FDTD), finite element method (FEM), and rigorous coupled wave analysis, to simulate the nano-scale structures. Ray tracing software (LightTools) was used with micrometer-scale 3D structures with thick layers.

Wu et al. conducted a series of studies on pixel OLEDs with 3D configurations [21–23]. In 2018, they extended mixed-level simulation to pixel OLEDs and proposed an effective pixel structure using high-index materials to fill the concave structures [21]. This research uses the analytical EM wave- and dipole-based power dissipation model to analyze the far-field emission properties of nano-scale layered structures without the NTFF method. In 2019, they analyzed the influence of the curvature of bank and shape of the filler on the efficiency and chromaticity [22]. In 2022, they conducted further experimental studies on previous pixel OLEDs and validated the previously presented simulations [23]. However, the devices they considered did not include BM and CF structures, and they also did not consider the light leakage effect. In addition, some other studies have analyzed of the performance of pixel OLEDs using only the EM method. Lee et al. used the FDTD method to analyze the light leakage between adjacent pixels [17]. Kang and Kim used FEM to investigate the effect of dipole orientation on the emission properties of pixel OLEDs with square boundaries [24]. However, due to the limitations of computation and time for large-sized cross-scale 3D OLEDs, optimizing them using the EM method is challenging.

To improve the resolution of OLED panels, full-color pixel structures comprising independent light-emitting RGB subpixels and CF arrays have been adopted (Fig. 1) [25,26]. The CF arrays filter the light leaked between adjacent pixels and alleviate the color shift of mixed light. However, the leaked light is trapped inside the device, which decreases the outcoupling efficiency. In this study, first, we constructed an optical model to simulate cross-scale 3D structures based on explicit wave optics and the 3D polarized ray tracing method, which could analyze the optical properties of pixel OLED devices. Then, we defined the ratio of light extraction (*RLE*) to evaluate the attenuation of intensity caused by the light leakage effect. Finally, after validating the model, we used pixel OLEDs with different sizes and examined the light leakage effect.

2. Theory and methods

2.1. Overview of the simulation model of pixel OLED

As shown in Fig. 1, cross-scale pixel OLEDs typically comprise nano- and micro-scale layered structures, including a filler, PDL, and glass. The main flow of the mixed-level algorithm was similar to that reported in previous literature; however, we made some improvements to make it more suitable for the optical simulation of pixel OLEDs. We adopted an analytical model based on wave optics to directly calculate the far-field spectrum of the nano-scale layered OLED device without using the NTFF method. In ray tracing (RT), the global coordinate system tracks the evolution of the propagate directions, and the local coordinate system describes the change in polarization. The calculation of the two coordinate systems was independent, and there was no interconversion between the two coordinate systems. The minor improvements in the algorithm are described in Sections 2.2 and 2.3.

As shown in Fig. 2, the flowchart of the mixed-level algorithm had three steps [20]. First, the source of ray optics in pixel OLEDs was determined by the far-field spectrum of the nano-scale layered structures. Second, the properties of surfaces were determined by reflectance and transmittance. Third, emission characteristics of the cross-scale 3D pixel OLEDs were determined using 3D polarized ray tracing with the results of the first two steps.

2.2. Modeling of nano-scale stratified structures based on wave optics

In our previous works, the explicit far-filled spectrum of layered anisotropic OLEDs was derived based on a radiation model of a dipole inside a microcavity, and this method was used to calculate the source of the ray optics [10]. The expression is given in Eq. (1):

$$I(\lambda,u)=\Theta\int_0^{1/n_d}K_{out}^{p,z}(\lambda,u)du+(1-\Theta)\int_0^{1/n_d}\left[K_{out}^{s,x}(\lambda,u)+K_{out}^{p,x}(\lambda,u)\right]du. \tag{1}$$

where, Θ is the dipole orientation parameter in the emitting layer (EML); n_d is the refractive of EML; K_{out} is the power dissipation function of the layered OLED; the superscripts "p" and "s" represent the p- and s-polarizations of the emission light, respectively; the superscripts "z" and "x" represent the vertically and horizontally oriented dipoles, respectively; λ is the wavelength; and u is the normalized horizontal wave vector. In ray tracing, Eq. (1) was rewritten as a function of viewing angle Ω in the filler, and it was given as Eq. (2) as follows:

$$I(\lambda,\Omega)=\frac{I(\lambda,u)}{2\pi n_d\tan\theta}, \tag{2}$$

herein, θ is emission angle, Ω is the solid angle.

The 4 × 4 matrix method is commonly used for calculating the reflectance and transmittance of interfaces [27–29]. The relationship between the electric field amplitude of the incident, reflected, and transmitted waves can be expressed using Eqs. (3) and (4):

$$\begin{bmatrix}E_{is} & E_{rs} & E_{ip} & E_{rp}\end{bmatrix}^T=\mathbf{\Gamma}\begin{bmatrix}E_{is} & 0 & E_{tp} & 0\end{bmatrix}^T, \tag{3}$$

$$\mathbf{TMM}=\mathbf{L}_i^{-1}\prod_{j=1}^{N}\mathbf{\Gamma}_j(-d_j)\mathbf{L}_t. \tag{4}$$

where, E represents the incident electric field amplitude, and the subscripts "i," "r," and "t" represent the incident, reflected, and transmitted waves, respectively. **TMM** is the transfer matrix, and it can be obtained by multiplying the inverse of incident matrix $\mathbf{L}_i^{-1}$, exit matrix $\mathbf{L}_t$, and partial transfer matrix of each layer $\mathbf{\Gamma}_j(-d_j)$. More details are available in

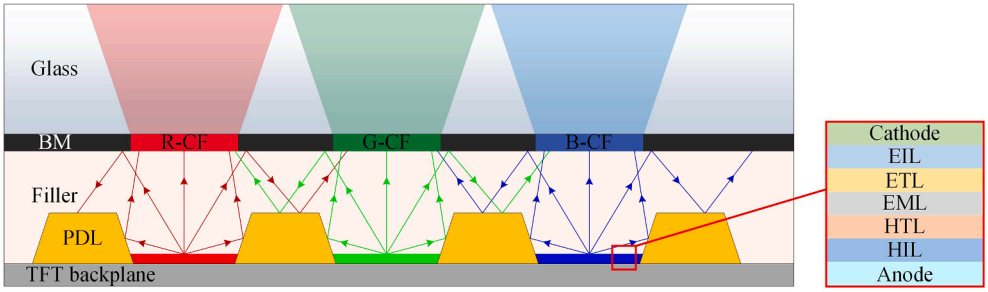

Fig. 1. Cross-section schematic of a typical pixel OLED with CF and BM structures.

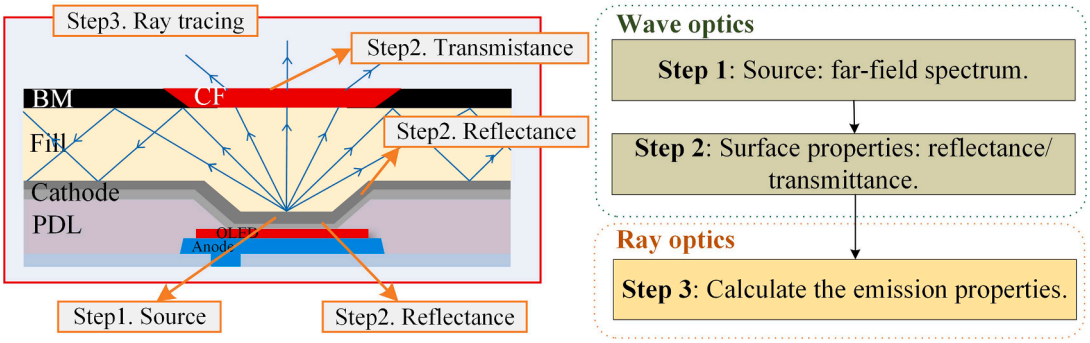

Fig. 2. Complete simulation flowchart of pixel OLEDs.

Ref. [28]. The reflectance and transmittance used in our model are expressed as $\mathbf{R} = [R_{ss}, R_{sp}, R_{pp}, R_{ps}]$ and $\mathbf{T} = [T_{ss}, T_{sp}, T_{pp}, T_{ps}]$, respectively.

2.3. Modeling of micro-scale 3D structures based on ray optics

A 2D ray tracing model analyzes the optical properties within a specific cross-section, and the polarization state of the light changes due to the anisotropic optical properties of the interface [30]. In this model, the relationship between the incident and reflected rays on a surface containing an anisotropic film in a micrometer-scale structure was expressed using Eq. (5):

$$\begin{aligned} \mathbf{I}_s^{\text{reflect}} &= \mathbf{I}_s^{\text{incident}}\mathbf{R}_{ss} + \mathbf{I}_p^{\text{incident}}\mathbf{R}_{ps}, \\ \mathbf{I}_p^{\text{reflect}} &= \mathbf{I}_p^{\text{incident}}\mathbf{R}_{pp} + \mathbf{I}_s^{\text{incident}}\mathbf{R}_{sp}. \end{aligned} \tag{5}$$

where, $\mathbf{I}$ is a vector comprising the radiant energy of rays in different angles, $\mathbf{R}$ is the vector of reflectance in different angles, and the subscripts "s" and "p" represent the TM-polarization generated by the incident TE-polarization. The relationship between the incident and transmitted rays was similar to that given using Eq. (5), and only reflectance was changed to transmittance. Some rays were reflected several times in the filler structure before exiting the device; hence, iterations of Eq. (5) were required.

The 2D ray tracing model is simple but is not sufficient for an asymmetric device. Unlike the 2D model, calculation in the 3D model involves the conversion of polarization states between different incident planes [31–33]. When rays were incident from plane 0 to planes 1 and 2 in succession, the polarization state changes were as shown in Fig. 3. The polarization of the incident and reflected rays of each plane was described by local coordinate systems, which were represented by different bases. The 0-th basis $\{\mathbf{s}_0, \mathbf{p}_0, \mathbf{k}_0\}$, 1-st basis $\{\mathbf{s}_1, \mathbf{p}_1, \mathbf{k}_1\}$, and 1′-st basis $\{\mathbf{s'}_1, \mathbf{p'}_1, \mathbf{k'}_1\}$ represent the local coordinate systems of the rays emitting from plane 0, incident on plane 1, and reflected by plane 1, respectively. The meaning of the remaining bases can be deduced using a similar logic. The vector $\mathbf{f}_i$ represents the normal vector of the ith plane. Changes in the polarization states between different incident planes were determined based on base conversion.

In the 3D ray tracing model, it was assumed that the radiant energy of rays with different polarizations under the basis $\{\mathbf{s}_0, \mathbf{p}_0, \mathbf{k}_0\}$ were I_0^s and I_0^p, and for the electric field were $\mathbf{E}_0^s = [1, 0, 0]$ and $\mathbf{E}_0^p = [1, 0, 0]$. The radiant energy of rays with different polarizations under the basis $\{\mathbf{s}_1, \mathbf{p}_1, \mathbf{k}_1\}$ were I_1^s and I_1^p, and for the electric field were $\mathbf{E}_1^s$ and $\mathbf{E}_1^p$. The electric field $\mathbf{E}_{0-1}$ of a ray incident from plane 0 to plane 1 was expressed using Eq. (6):

$$\mathbf{E}_{0-1}^{s/p} = \{\mathbf{s}_1, \mathbf{p}_1, \mathbf{k}_1\}\mathbf{E}_1^{s/p} = \{\mathbf{s}_0, \mathbf{p}_0, \mathbf{k}_0\}\mathbf{C}\mathbf{E}_1^{s/p} = \{\mathbf{s}_0, \mathbf{p}_0, \mathbf{k}_0\}\mathbf{E}_0^{s/p}. \tag{6}$$

Therefore, the conversion between electric fields under two bases was expressed using Eq. (7):

$$\mathbf{E}_1^{s/p} = \mathbf{C}^{-1}\mathbf{E}_0^{s/p}. \tag{7}$$

where, $\mathbf{C}$ is the transition matrix:

$$\mathbf{C} = \{\mathbf{s}_0, \mathbf{p}_0, \mathbf{k}_0\}^{-1}\{\mathbf{s}_1, \mathbf{p}_1, \mathbf{k}_1\}. \tag{8}$$

In the 3D ray tracing of the pixel OLED, the ray propagation vector $\mathbf{k}$ and the normal vector of the plane $\mathbf{f}$ were known, and the remaining components in the 0-th and 1-st bases were expressed using Eqs. (9)–(13):

$$\mathbf{s}_0 = \frac{\mathbf{k}_0 \times \mathbf{f}_0}{|\mathbf{k}_0 \times \mathbf{f}_0|}, \tag{9}$$

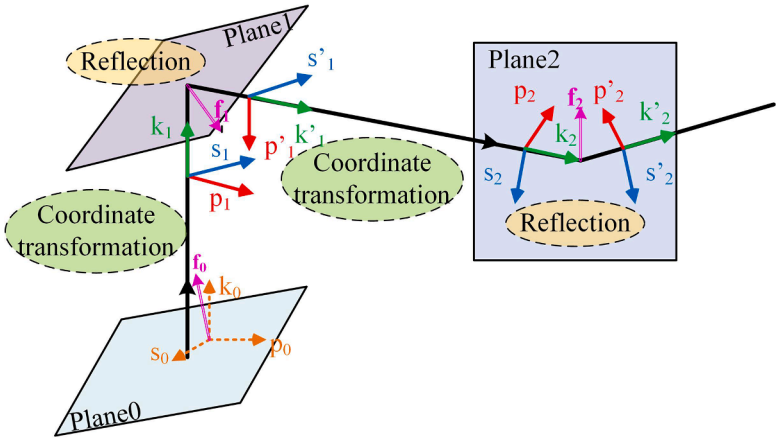

Fig. 3. Schematic diagram of 3D polarized ray tracing.

$$\mathbf{p}_0 = \frac{\mathbf{k}_0 \times \mathbf{s}_0}{|\mathbf{k}_0 \times \mathbf{s}_0|}, \tag{10}$$

$$\mathbf{s}_1 = \frac{\mathbf{k}_1 \times \mathbf{f}_1}{|\mathbf{k}_1 \times \mathbf{f}_1|}, \tag{11}$$

$$\mathbf{p}_1 = \frac{\mathbf{k}_1 \times \mathbf{s}_1}{|\mathbf{k}_1 \times \mathbf{s}_1|}, \tag{12}$$

$$\mathbf{k}_1 = \mathbf{k}_0. \tag{13}$$

Radiant energy is proportional to the square of the electric field amplitude; therefore, the relationship between the radiant energy in different bases was expressed using Eq. (14):

$$\begin{aligned} I_1^s &= \frac{I_0^s \cdot \left(\mathbf{E}_1^s(1)\right)^2}{\left(\mathbf{E}_1^s(1)\right)^2 + \left(\mathbf{E}_1^s(2)\right)^2} + \frac{I_0^p \cdot \left(\mathbf{E}_1^p(1)\right)^2}{\left(\mathbf{E}_1^p(1)\right)^2 + \left(\mathbf{E}_1^p(2)\right)^2}, \\ I_1^p &= \frac{I_0^s \cdot \left(\mathbf{E}_1^s(2)\right)^2}{\left(\mathbf{E}_1^s(1)\right)^2 + \left(\mathbf{E}_1^s(2)\right)^2} + \frac{I_0^p \cdot \left(\mathbf{E}_1^p(2)\right)^2}{\left(\mathbf{E}_1^p(1)\right)^2 + \left(\mathbf{E}_1^p(2)\right)^2}. \end{aligned} \tag{14}$$

where, $\mathbf{E}(j)$ represents the jth element in the vector $\mathbf{E}$. When rays were incident on plane 1, the incident plane and the polarization of the rays in the local coordinate system did not change. The energy of the reflected ray was calculated using Eq. (5), and the base changes from $\{\mathbf{s}_1, \mathbf{p}_1, \mathbf{k}_1\}$ to $\{\mathbf{s}'_1, \mathbf{p}'_1, \mathbf{k}'_1\}$ were given using Eqs. (15) and (16):

$$\mathbf{s}'_1 = \frac{\mathbf{k}'_1 \times \mathbf{f}_1}{|\mathbf{k}'_1 \times \mathbf{f}_1|}, \tag{15}$$

$$\mathbf{p}'_1 = \frac{\mathbf{k}'_1 \times \mathbf{s}_1}{|\mathbf{k}'_1 \times \mathbf{s}_1|}. \tag{16}$$

where, $\mathbf{k}'_1$ is the propagation vector of the reflected ray, and it can be easily obtained using the law of refraction. When the ray was incident from plane 1 to plane 2 again, the above process was repeated.

Most of the filler layers in pixel OLEDs are transparent; however, some materials exhibit slight absorption for short wavelength. Thus, it is necessary to consider the attenuation of amplitude in the medium. According to Lambert's law [34], ray energy attenuation can be expressed using Eq. (17):

$$I = I_0 e^{-\alpha_a l}. \tag{17}$$

where, I_0 and I represent the ray energy at x=0 and x=l, respectively, and α_a is the absorption coefficient (calculated using Eq. (18)).

$$\alpha_a = \frac{2k\omega}{c} = \frac{4\pi k}{\lambda}. \tag{18}$$

2.4. Evaluation of the light leakage effect

The method described in Sections 2.1–2.3 was used to calculate the properties of cross-scale 3D pixel OLEDs, which included the angle-dependent CIE 1931 color coordinates (*CIEx* and *CIEy*), normalized intensity (*Norm.Intensity*), normalized current efficiency (*Norm.CE*), and the attenuation of intensity caused by the light leakage effect. In the light leakage effect, light at a subpixel level propagates to the adjacent subpixel along the optical path between the BM and the PDL. In this study, the CFs of the adjacent subpixels were different, and light leaking to the adjacent pixels was filtered by the CFs. This only slightly influenced the performance of the adjacent pixel and led to the attenuation of the light intensity of that subpixel. The ratio of light extraction (*RLE*) was defined to analyze the attenuation of intensity caused by the light leakage effect, and it was calculated using Eq. (19).

$$RLE = \frac{\sum_{j=1}^{M} \sum_{i=1}^{N'} \int_{380}^{780} I(\lambda, \theta_i) \cdot T(\lambda, \theta_i) d\lambda}{\sum_{i=1}^{N} \int_{380}^{780} I(\lambda, \theta_i) d\lambda}. \tag{19}$$

where, $I(\lambda,\theta_i)$ is the far-field energy of the ray from the source when the wavelength is λ, and the angle is θ_i. $T(\lambda,\theta_i)$ is the transmittance when the wavelength is λ, and the angle is θ_i. N is the number of source rays, N' is the number of detected rays, and M is the number of times the rays are reflected in the pixel device.

3. Results and discussion

Based on the mixed-level algorithm and evaluation of the light leakage effect, the custom MATLAB codes were written to implement the optical simulation of cross-scale pixel OLED devices. First, the accuracy and efficiency of the model were verified using two commercial software, namely ExpertRT and ExpertOLED. Then, considering the light leakage effect, the properties of cross-scale pixel OLEDs with different sizes were analyzed.

3.1. Verification of the validity of the proposed model

Wave optics models have been verified in previous studies [10,11,28]. Herein, the ray optics model of the mixed-level algorithm was verified using commercial software ExpertRT and ExpertOLED2D (LINKGLOBAL21 CO., LTD.). First, a simple trapezoid structure was taken, as shown in Fig. 4(a). This structure was described as a trapezoidal glass (n = 1.5, k = 0) surrounded by air (n = 1.0, k = 0). In the simulation, the number of rays was 1000, and an s-polarization source with a wavelength of 450 nm was considered. Detectors were located at the top of the structure, and the angular resolution of ExpertRT 2D was 0.001. The emission intensity profiles are shown in Fig. 4(b). The ray tracing results of our model were consistent with those of ExpertRT 2D, which verified the correctness of the proposed model. For ExpertRT, smaller angular resolutions resulted in higher accuracy. We compared the time required for simulating 5000 rays with the angular resolution of 0.00001. The time required by ExpertRT and our model were 8 and 1.5 min, respectively, that is, time required by our model was 1/5 times less than that of ExpertRT.

Further, we verified the accuracy of the mixed-level algorithm with ExpertOLED 2D (LINKGLOBAL21 CO., LTD.), which uses the FDTD theory. The structure used for this part is presented in Fig. 5. In the FDTD simulation, we set up 11 dipoles with different positions evenly distributed in the center of the Alq3 layer, and the orientation was horizontal. The detector was on top of the device. The optical constants (including refractive index and extinction coefficient) used were as given in a previous study [10].

Fig. 6 shows the angle-resolved *Norm.Intensity* of our model and ExpertOLED 2D at different viewing angles (0–80°). Some differences were noted in the simulation results between our model and ExpertOLED because of the difference in their principles. In our model, the nanometer-scale structure was calculated by physical optics, and the micrometer-scale structure was calculated by ray optics. ExpertOLED adopted the FDTD method to calculate the whole structure. At smaller viewing angles, the direct out-coupled light dominated the emission spectrum, which was more suitable for FDTD. At larger viewing angles, the contribution of light extracted by the reflective became more prominent, resulting in increased optical path and decreased coherence, which was more suitable for the ray tracing method. The simulated results obtained by the mixed-level algorithm described the shape of the spectra obtained using the FDTD. The *Norm.Intensity* obtained by FDTD showed interference modulation associated with the thick filler layer. The mixed-level algorithm only considered the ray optics features in the micro-scale structure and could not obtain partial interference

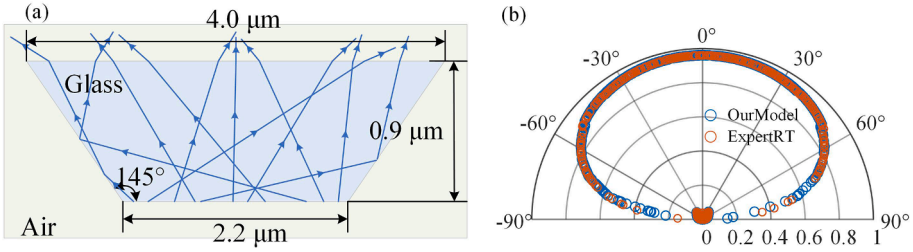

Fig. 4. Verification of the ray tracing model with ExpertRT 2D: (a) basic structure used in simulation; (b) comparison of the emission intensity profile with wavelength of 450 nm.

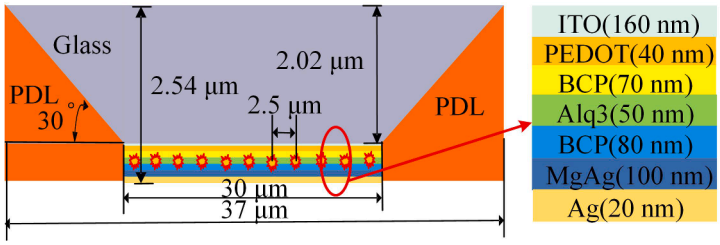

Fig. 5. Structure used for verifying the mixed-level algorithm with ExpertOLED.

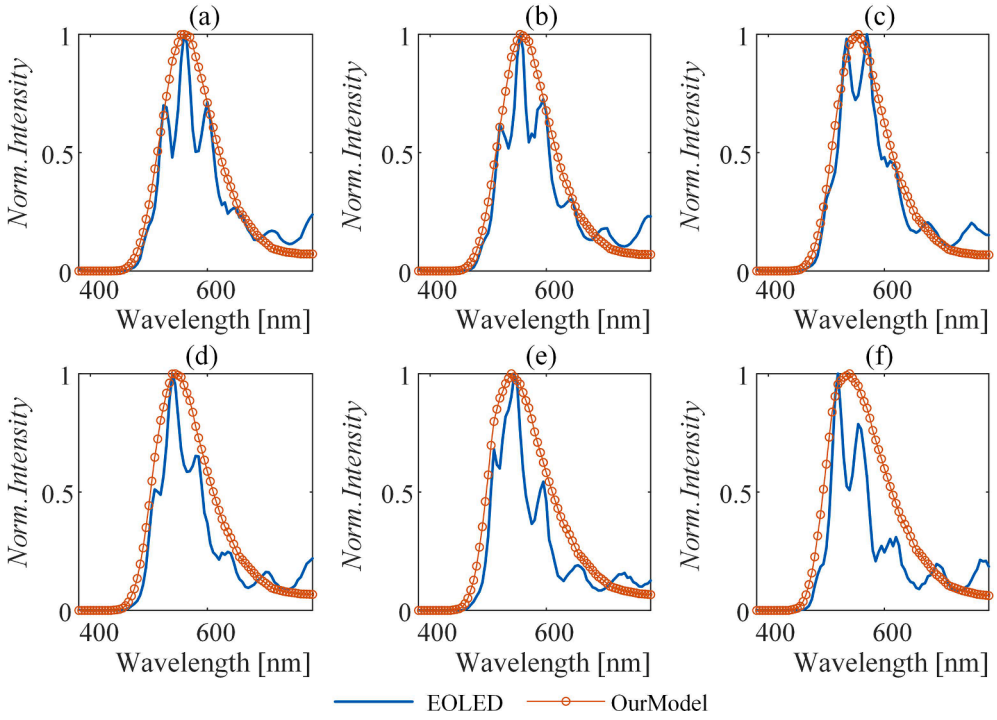

Fig. 6. Normalized intensity of our model and ExpertOLED at different viewing angles: (a) 0°; (b) 15°; (c) 30°; (d) 45°; (e) 60°; (a) 75°.

modulation; therefore, the spectral profiles were smooth. While there was some deviation in the *Norm.Intensity*, the evaluation of performance trends, such as *Norm.CE* and *CIE*, was unaffected, as shown in Fig. 7. The trend of *Norm.CE* first increased and then decreased, reaching a maximum at 40°. The color shift of the two simulations reached the maximum at 70°.

3.2. *Influence of micro-scale structure on pixel OLED performance*

Using the above models, the influence of the light leakage effect on the performance of cross-scale pixel OLEDs could be quickly analyzed. We considered a typical green subpixel with CF and BM as an example, as shown in Fig. 8. It is a symmetric structure, and only the structure in the *xz* plane is shown. The layers of the emission structure were a filler (incoherent), / capping layer (CPL 60 nm) / MgAg (15 nm) / electron transport layer (ETL 30 nm) / emissive layer (EML 30 nm) / hole transport layer (HTL 15 nm) / hole injection layer (HIL 160 nm) / ITO (15 nm) / Ag (100 nm) / ITO (10 nm). The optical constants (including refractive index and extinction coefficient) and thickness required for the simulation of each layer were measured using a spectroscopic ellipsometer (ME-L, Wuhan E-optics Technology Co.) [35,36]. The optical constants of the materials of each layer with the wavelength λ of 540 nm are shown in Table 1. In the simulation, the dipoles were located in the middle of EML, and the orientation was horizontal. The current

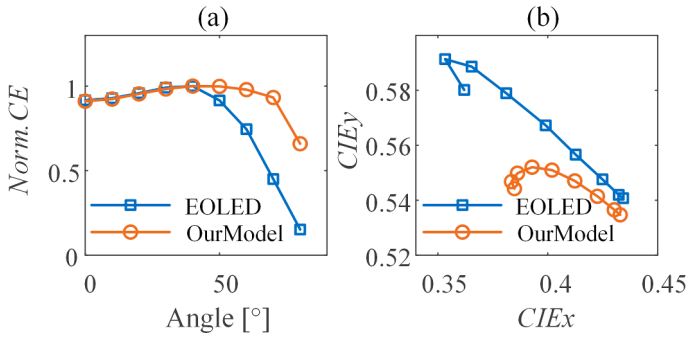

Fig. 7. Trend of device performance at different angles: (a) *Norm.CE*; (b) angle-dependent CIE 1931 color coordinates.

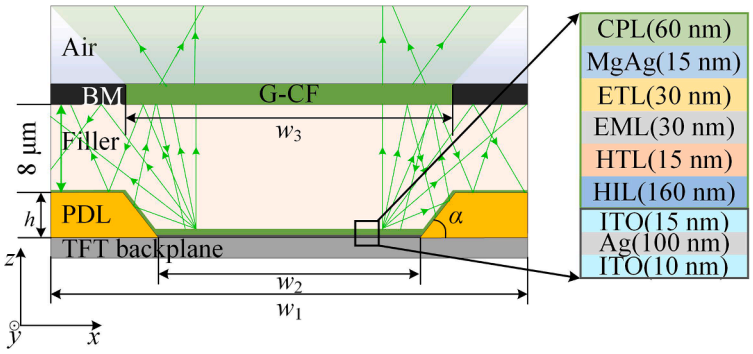

Fig. 8. Structure of a typical green subpixel OLED with CF and BM.

Table 1
Optical constants of OLED layers at wavelength $\lambda = 540$ nm.

	ITO	Ag	HIL	HTL	EML	ETL	Mg:Ag	CPL	CF	BM	Filler	PDL
n	1.904	0.078	1.770	1.730	1.780	1.746	0.014	1.260 (n_o) 1.265 (n_e)	1.610	1.822	1.488	1.714
k	0	3.334	0	0	0	0	3.257	0	0.006	0.447	0	0.013

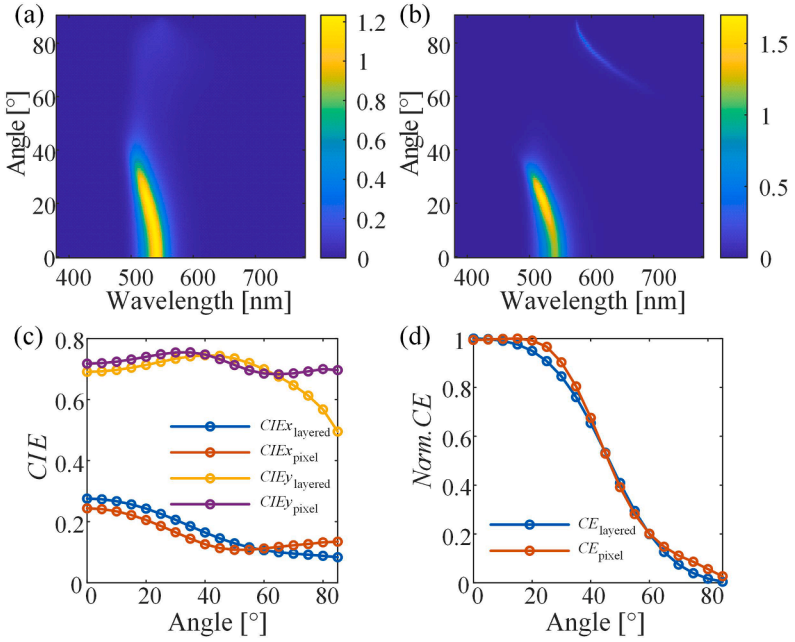

Fig. 9. (a) Angle-resolved TE far-field spectra in the filler layer; (b) angle-resolved TM far-field spectra in the filler layer; (c) angle-dependent CIE 1931 color coordinates; (d) normalized intensity of the equivalent layered OLED and pixel OLED ($w_1 = 140$ μm, $w_2 = 80$ μm, $w_3 = 80$ μm, $h = 2$ μm, and $\alpha = 30°$).

density was $I_{inj} = 10$ mA/cm^2. Other parameters needed in the simulation were all set to 1.

The far-field spectra in the filler layer are shown in Fig. 9(a and b), which was also the ray tracing source. When the viewing angle was >40°, the intensity was close to zero. The peak wavelength of the spectrum at 0° was 561 nm, and it was blue-shifted as the viewing angle increased. The interface in the pixel OLED was divided into five categories, namely, BM, CF, perfect matching layer, PDL, and layered OLED interface. The reflectance and transmittance were calculated using the 4 × 4 matrix method. Total internal reflection (TIR) occurred when the incident angle was greater than the critical angle because $n_{Filler} > n_{air}$. In addition, the PDL structure was simplified to a semi-infinite structure. Only the reflection of light on the interface surface of PDL was considered, while the transmission of light inside the PDL structure was ignored.

First, we compared the optical performance of the cross-scale pixel OLED with an equivalent layered OLED. The 2D mixed-level algorithm model was used in this part to make the simulation less complex and time-consuming. The structure of the equivalent layered OLED comprised air (incoherent) / CPL (60 nm) / MgAg (15 nm) / ETL (30 nm) / EML (30 nm) / HTL (15 nm) / HIL (160 nm) / ITO (15 nm) / Ag (100 nm) / ITO (10 nm). The color coordinates and normalized intensity of the equivalent layered OLED and pixel OLED ($w_1 = 140$ μm, $w_2 = 80$ μm, $w_3 = 80$ μm, $h = 2$ μm, and $\alpha = 30°$) are shown in Fig. 9(c and d). The color shift of pixel OLED was less than that of the layered OLED, which was caused by the filtering of CFs as well as the rays reflected by the PDL. Furthermore, the normalized intensity decay rates of the pixel OLEDs at small and large angles (<20° and >60°, respectively) were less than those of the equivalent layered OLEDs. Thus, the angle-dependent characteristics of the device were mitigated by using a PDL, BM, and CF structure in the pixel OLED. The actual intensity of the pixel OLED was less than that of the layered OLED due to the light leakage effect in pixel OLED, the filtering effect of CF, and the TIR. Similar to *RLE*, the ratio of the actual intensity of pixel OLED to that of layered OLED was 67.56%. It was calculated by replacing the far-field intensity of the light source in the denominator with the far-field intensity of the layered OLED device.

Further, three different sizes of cross-scale pixel OLEDs were simulated to investigate the effect of variations in the width of the CF(w_3) and the angle and the height of the PDL (α and h) on OLED performance. The dimensions of each device are shown in Table 2. The variations of *RLE* are shown in Fig. 10(a–c) with varying h and α and fixed w_3 (for each device, w_3 and w_2 were the same). The *RLE*s of the three devices were in the order $RLE_B > RLE_A > RLE_C$. For device B, *RLE* decreased as α increased, while h had less effect on the *RLE*. In contrast, for devices A and C, α had less influence on the *RLE*, and it decreased as h increased. The color shift of the pixel OLED was slight for the filtering effect of CF. Thus, only the *CIE* at the normal angle of each device is shown in Fig. 10 (d–f). The variation of h had a negligible effect on the chromaticity of devices A, B, and C. In contrast, α significantly affected the color coordinates, and the chromaticity of the three devices showed the same trend as the angle increased. The *CIE* of device B showed the most considerable magnitude change with changes in α, which indicated that it was more sensitive to α.

Thus, the influence of the micro-scale structure on the performance was different for pixel OLEDs with different sizes, which were attributed to the different sensitivities of different sizes to changes in micro-scale structures. For device A, the width of the organic layer (w_1) was considerably larger than the height of the PDL (h); as a result, the proportion of ray incident to the PDL structure was smaller, and most of the rays exited directly into the air through the CF. For device B, w_1 was smaller than that for device A, and the geometric features of the pixel were more pronounced. The proportion of the rays incident to the PDL structure increased, and these rays were reflected by the PDL and then exited into the air through the CF. Thus, RLE_B was > RLE_A, and the performance was more sensitive to changes in the micro-scale structure. For device C, w_1 and h were comparable, and the proportion of rays incident on the PDL structure was the largest. Some rays were repeatedly reflected in the pixel structure and leaked into adjacent subpixels instead of exiting into the air. Therefore, RLE_C was minimum.

Finally, we analyzed the variation of CF width (w_3) on the *RLE* of the three devices. h and α were set to 2 μm and 60°, respectively. As shown in Fig. 11, the *RLE* of each device increased with the increase in w_3. This was because a wider CF enabled more light to exit directly into the air, avoiding energy loss caused by rays reflected by the BM and then leaking into the adjacent pixels. Theoretically, narrower width of the BM implied lesser light leakage. However, since BM was used to avoid RGB color mixing and shading, it played an important role in display panels; thus, the width of BM was limited to some extent. In general, the width of BM depends on the process conditions. The above multivariable simulations for pixel OLEDs were challenging to be completed by FDTD because it is a time-consuming process. In Section 3.1, the simulation of a structure with ExpertOLED was completed in nearly 1 h. Multivariable simulations of devices A, B, and C with ExpertOLED would be more time-consuming and almost impossible to complete.

Table 2
The dimensions of the cross-scale pixel OLEDs.

Device	w_1 [μm]	w_2 [μm]	w_3 [μm]	h [μm]	α [°]
A	w_2+2 h/tan (α)+10	80	[w_2/2, w_2+2 h/tan (α)] (step: 4 μm)	2, 7, 12	15°–75° (step:5°)
B		40			
C		20			

3. Conclusions

In this study, an optical simulation model was proposed to enable rapid analysis of the performance of cross-scale pixel OLEDs, and an evaluation parameter of the light leakage effect was defined. The model was based on a mixed-level algorithm, which considered wave and ray optics. An analytical model based on wave optics was used to directly calculate the far-field spectra of the layered OLED. In RT, the global coordinate system was used to track the propagation directions of rays, and the local coordinate system described the polarization change. The calculations of the two coordinate systems were independent, and there were no interconversions between them, which was more convenient for code implementation. Based on the proposed model, the properties of the cross-scale pixel OLEDs considering the light leakage effect were analyzed using a custom MATLAB code. The PDL, BM, and CF effectively suppressed the angle-dependent performance of pixel OLEDs. Moreover, the PDL angle (α) significantly influenced the *CIE* of devices A, B, and C and RLE_B. The PDL height (h) only influenced RLE_A and RLE_C. In addition, the *RLE* of each device increased as w_3 increased, illustrating decreased light leakage. Device B had the least light leakage effect. These results demonstrate that the proposed model provides a systematic method for analyzing the performance of pixel OLEDs, and the reasonable design of micro-scale structures is beneficial for improving device quality. This method has excellent application prospects in pixel OLED design.

Funding

This work was supported by the National Natural Science Foundation of China [52130504, 51727809], Key Research and Development Plan of Hubei Province [2021BAA013], Natural Science Foundation of Hubei Province [2021CFB322], and the Fundamental Research Funds for the Central Universities [2021XXJS113].

CRediT authorship contribution statement

Linya Chen: Methodology, Formal analysis, Investigation, Writing –

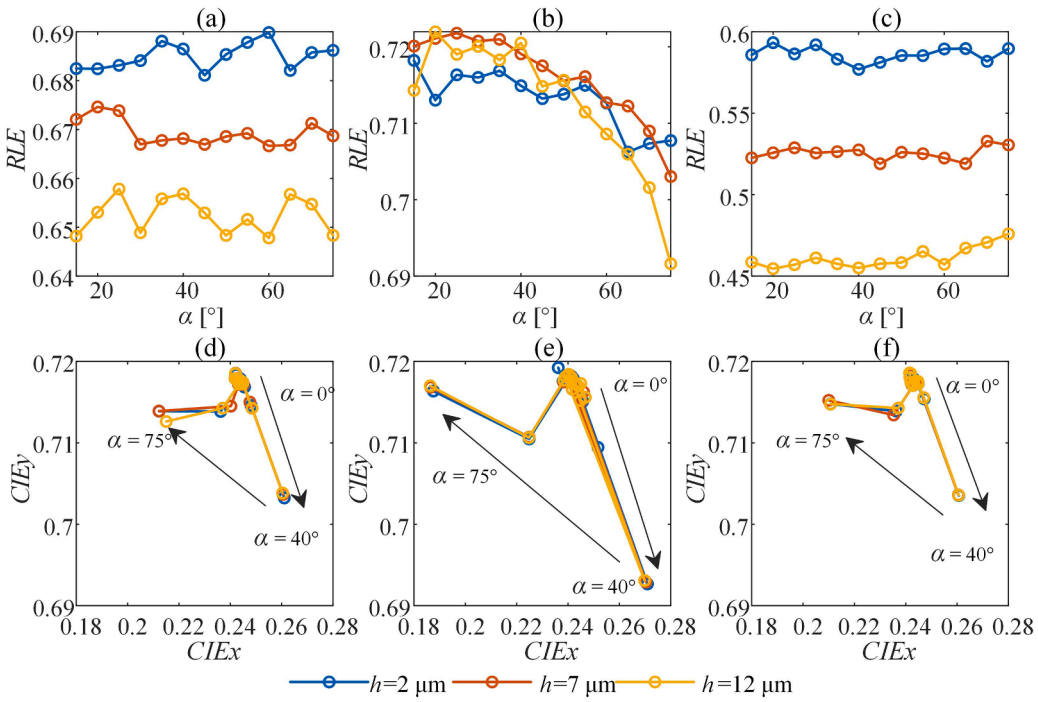

Fig. 10. Influence of variation in PDL height (h) and angle (α) on the performance of pixel OLED: (a) RLE_A; (B) RLE_B; (c) RLE_C; (d) CIE_A; (e) CIE_B; (f) CIE_C.

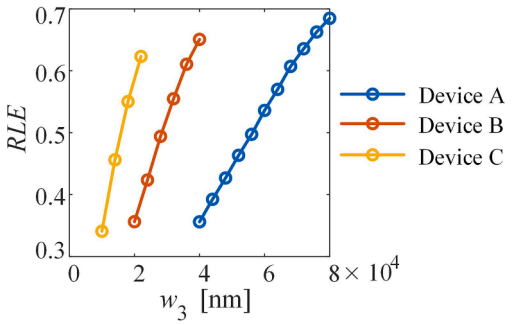

Fig. 11. Influence of variation of CF width (w_3) on the *RLE* of pixel OLEDs.

original draft. **Honggang Gu:** Conceptualization, Methodology, Writing – review & editing, Supervision, Project administration, Funding acquisition. **Shibo Jiao:** Validation, Formal analysis, Writing – review & editing. **Shiyuan Liu:** Writing – review & editing, Supervision, Project administration, Funding acquisition.

Declaration of Competing Interest

The authors declare that they have no known competing financial interests or personal relationships that could have appeared to influence the work reported in this paper.

Data availability

Data will be made available on request.

Acknowledgments

The authors thank the technical support from the Experiment centre for Advanced Manufacturing and Technology in School of Mechanical Science &Engineering of HUST.

References

[1] S.J. Zou, Y. Shen, F.M. Xie, J.D. Chen, Y.Q. Li, J.X. Tang, Recent advances in organic light-emitting diodes: toward smart lighting and displays, Mater. Chem. Front. 4 (2020) 788–820.
[2] G. Huseynova, J.H. Lee, Y.H. Kim, J. Lee, Transparent organic light-emitting diodes: advances, prospects, and challenges, Adv. Opt. Mater. 9 (2021), 2002040.
[3] J. Song, H. Lee, E.G. Jeong, K.C. Choi, S. Yoo, Organic light-emitting diodes: pushing toward the limits and beyond, Adv. Mater. 32 (2020), e1907539.
[4] L. Yu, Y. Su, F. Yang, Y. Yang, F. Liu, G. Zhou, Review on theories of electrical physics in OLEDs, Chin. J. Liq. Cryst. Disp. 37 (2022) 980–996.
[5] J. Kim, J. Kim, Theoretical modeling and analysis of the contribution of the near-field absorption to the dipole radiation power in top-emitting organic light-emitting diodes, Appl. Sci. 11 (2021) 3181.
[6] S.K. Kim, S.W. Jung, H.U. Park, R. Lampande, J.H. Kwon, Accurate optical simulation method of tandem organic light-emitting diode with consideration of Purcell effect, Org. Electron. 95 (2021), 106192.
[7] C.Y. Chan, M. Tanaka, Y.T. Lee, Y.W. Wong, H. Nakanotani, T. Hatakeyama, C. Adachi, Stable pure-blue hyperfluorescence organic light-emitting diodes with high-efficiency and narrow emission, Nat. Photonics 15 (2021) 245.
[8] Y. Gu, D.D. Zhang, Q.D. Ou, Y.H. Deng, J.J. Zhu, L. Cheng, Z. Liu, S.T. Lee, Y.Q. Li, J.X. Tang, Light extraction enhancement in organic light-emitting diodes based on localized surface plasmon and light scattering double-effect, J. Mater. Chem. C 1 (2013) 4319–4326.
[9] K. Kang, Y. Lee, J. Kim, H. Lee, B. Yang, A Generalized Fabry–Pérot formulation for optical modeling of organic light-emitting diodes considering the dipole orientation and light polarization, IEEE Photonics J. 8 (2016) 1–19.
[10] X. Ke, H. Gu, X. Zhao, X. Chen, Y. Shi, C. Zhang, H. Jiang, S. Liu, Simulation method for study on outcoupling characteristics of stratified anisotropic OLEDs, Opt. Express 27 (2019) A1014–A1029.
[11] X. Ke, H. Gu, L. Chen, X. Zhao, J. Tian, Y. Shi, X. Chen, C. Zhang, H. Jiang, S. Liu, Multi-objective collaborative optimization strategy for efficiency and chromaticity of stratified OLEDs based on an optical simulation method and sensitivity analysis, Opt. Express 28 (2020) 27532–27546.
[12] E. Kim, J. Chung, J. Lee, H. Cho, N.S. Cho, S. Yoo, A systematic approach to reducing angular color shift in cavity-based organic light-emitting diodes, Org. Electron. 48 (2017) 348–356.
[13] H.S. Jeon, B. Pyo, H. Park, S.R. Park, M.C. Suh, Improved out-coupling efficiency of organic light emitting diodes by manipulation of optical cavity length, Org. Electron. 20 (2015) 49–54.
[14] H. Cho, C.W. Joo, S. Choi, C.m. Kang, G.H. Kim, J.W. Shin, B.H. Kwon, H. Lee, C. W. Byun, N.S. Cho, Design of white tandem organic light-emitting diodes for full-color microdisplay with high current efficiency and high color gamut, ETRI J. 43 (2021) 1093–1102.
[15] S. Sim, J. Ryu, D.H. Ahn, H. Cho, C.M. Kang, J.W. Shin, C.W. Joo, G.H. Kim, C. W. Byun, N.S. Cho, H.M. Youn, Y.J. An, J.S. Kim, H. Jung, H. Lee, Color gamut change by optical crosstalk in high-resolution organic light-emitting diode microdisplays, Opt. Express 30 (2022) 24155.

[16] C.M. Kang, J.W. Shin, S. Choi, B.H. Kwon, H. Cho, N.S. Cho, J.I. Lee, H. Lee, J. H. Lee, H. Kim, A. Cho, S.H. Park, M. Kim, S.G. Park, Y. Kim, J. Ha, J. Kim, S. T. Kim, J.S. Lee, S.N. Lee, Y.B. Im, C.W. Byun, High aspect ratio microdisplay and thin optical component for glass-like AR devices, J. Inf. Disp. 22 (2021) 163–171.
[17] J.K. Lee, S. Cho, D.W. Kang, Analysis of light leakage between the adjacent pixels in a color-filter stacked white OLED display, Displays 45 (2016) 6–13.
[18] F. Gou, E.L. Hsiang, G. Tan, P.T. Chou, P.T. Chou, Y.L. Li, Y.F. Lan, S.T. Wu, Angular color shift of micro-LED displays, Opt. Express 27 (2019) A746–A757.
[19] K.D. Chang, C.Y. Li, J.W. Pan, K.Y. Cheng, A hybrid simulated method for analyzing the optical efficiency of a head-mounted display with a quasi-crystal OLED panel, Opt Express 22 (2014) A567–A576.
[20] M.H. Kane, J. Jiao, N. Dietz, J.J. Huang, M. Bahl, G.R. Zhou, E. Heller, W. Cassarly, M. Jiang, R. Scarmozzino, G.G. Gregory, Optical simulations of organic light-emitting diodes through a combination of rigorous electromagnetic solvers and Monte Carlo ray-tracing methods, in: Proceedings of the Thirteenth International Conference on Solid State Lighting, SPIE Proc 9190, 2014, p. 09, https://doi.org/10.1117/12.2061089.
[21] Y.J. Chen, W.K. Lee, Y.T. Chen, C.Y. Lin, S.W. Wen, M. Jiao, G.D. Su, H.Y. Lin, R. J. Visser, B.L. Kwak, C.C. Chen, W.Y. Lin, S. Wang, C.P. Chang, C.C. Wu, A vision toward ultimate optical out-coupling for organic light-emitting diode displays: 3D pixel configuration, Adv. Sci. 5 (2018), 1800467.
[22] W.K. Lee, Y.T. Chen, S.W. Wen, P.H. Liao, M.C. Lee, T.S. Hsu, Y.J. Chen, G.D. Su, H. Y. Lin, C.C. Chen, W.Y. Lin, L. Xu, G. Yu, B.L. Kwak, R.J. Visser, C.C. Wu, Three-dimensional pixel configurations for optical outcoupling of OLED displays-optical simulation, J. Soc. Inf. Disp. 27 (2019) 273–284.
[23] Y.T. Chen, S.W. Wen, P.H. Liao, W.K. Lee, C.C. Lee, C.W. Huang, Y.H. Yang, K. C. Lin, C.J. Chang, G.D. Su, H.Y. Lin, C.C. Chen, W.Y. Lin, B.L. Kwak, R.J. Visser, C. C. Wu, Reflective 3D pixel configuration for enhancing efficiency of OLED displays, Org. Electron. 103 (2022), 106451.
[24] K. Kang, J. Kim, Effect of dipole orientation on the angular emission characteristic of a three-dimensional top-emitting organic light-emitting diode with square pixel boundary, J. Korean Phys. Soc. 74 (2019) 649–659.
[25] A. Chida, T. Aoyama, S. Eguchi, T. Inoue, N. Senda, T. Sakuishi, H. Ikeda, S. Shitagaki, N. Ohsawa, H. Inoue, K. Suzuki, H. Seo, T. Sasaki, Y. Nonaka, H. Nakashima, T. Suzuki, T. Watabe, S. Seo, Y. Hirakata, S. Yamazaki, S. Yasumoto, M. Sato, Y. Yasuda, S. Okazaki, W. Nakamura, S. Mitsui, Flexible high-resolution full-color top-emitting active-matrix organic light-emitting diode display, J. Soc. Inf. Disp. 21 (2013) 422–432.
[26] R. Yamaoka, T. Sasaki, R. Kataishi, N. Miyairi, K. Kusunoki, M. Kaneyasu, H. Miyake, N. Ohsawa, S. Seo, Y. Hirakata, S. Yamazaki, K. Ono, T. Cho, H. Mori, High-resolution OLED display with remarkably low power consumption using blue/yellow tandem structure and RGBY subpixels, J. Soc. Inf. Disp. 23 (2015) 451–456.
[27] K. Kang, S. Lee, J. Kim, S. Kim, Y. Han, S. Baek, A simple numerical modeling of the effect of the incoherent thick substrate in thin-film solar cells based on the equispaced thickness method, IEEE Photonics J. 8 (2016) 1–12.
[28] X. Zhao, R. Xia, H. Gu, X. Ke, Y. Shi, X. Chen, H. Jiang, H.L. Yip, S. Liu, Performance optimization of tandem organic solar cells at varying incident angles based on optical analysis method, Opt. Express 28 (2020) 2381–2397.
[29] M.C. Troparevsky, A.S. Sabau, A.R. Lupini, Z. Zhang, Transfer-matrix formalism for the calculation of optical response in multilayer systems: from coherent to incoherent interference, Opt. Express 18 (2010) 24715–24721.
[30] A.C. Wei, J.R. Sze, Modeling OLED lighting using Monte Carlo ray tracing and rigorous coupling wave analyses, Opt. Commun. 380 (2016) 394–400.
[31] G. Yun, K. Crabtree, R.A. Chipman, Three-dimensional polarization ray-tracing calculus I: definition and diattenuation, Appl. Opt. 50 (2011) 2855–2865.
[32] G. Yun, S.C. McClain, R.A. Chipman, Three-dimensional polarization ray-tracing calculus II: retardance, Appl. Opt. 50 (2011) 2866–2874.
[33] H. Zhang, Y. Li, C. Yan, J. Zhang, Three-dimensional polarization ray tracing calculus for partially polarized light, Opt. Express 25 (2017) 26973–26986.
[34] T. Basak, Analysis of microwave propagation for multilayered material processing: Lambert's law versus exact solution, Ind. Eng. Chem. Res. 43 (2004) 7671–7675.
[35] S. Liu, X. Chen, C. Zhang, Development of a broadband Mueller matrix ellipsometer as a powerful tool for nanostructure metrology, Thin Solid Films 584 (2015) 176–185.
[36] H. Gu, X. Chen, H. Jiang, S. Liu, Optimal broadband Mueller matrix ellipsometer using multi-waveplates with flexibly oriented axes, J. Opt. 18 (2016), 025702.